bioengineering

MDPI

Article

Ring-Array Ultrasound Computed Tomography for Musculoskeletal Tissue Imaging: System Design and Key Methods

Chao Wu [1], Guangquan Zhou [2], Chuan Chen [2], Zihan Long [2], Wansu Fu [2], Ximin Yang [2], Libo Sun [1] and Wenhu Qin [1,*]

[1] School of Instrument Science and Engineering, Southeast University, Nanjing 210096, China; chaowu@seu.edu.cn (C.W.); sunlibo@seu.edu.cn (L.S.)
[2] School of Biological Science and Medical Engineering, Southeast University, Nanjing 210096, China; guangquan.zhou@seu.edu.cn (G.Z.); chuanchen@seu.edu.cn (C.C.); 220252550@seu.edu.cn (Z.L.); fuws52@seu.edu.cn (W.F.); anton_h_yang@163.com (X.Y.)
* Correspondence: qinwenhu@seu.edu.cn

Abstract

Conventional handheld ultrasound provides localized, single-sided views of limb musculoskeletal structures. Examination quality is highly operator-dependent because probe position, beam incidence angle, acoustic-window selection, and contact pressure vary with technique, reducing spatial reproducibility. Moreover, acoustic heterogeneity causes sound-speed mismatch and focusing errors. To address these limitations, we developed a fixed ring-array ultrasound computed tomography (USCT) system for complete cross-sectional imaging and three-dimensional reconstruction. It integrates a 512-element ring array, 128-channel electronics, and mechanical axial scanning. A dataset-specific global effective sound speed was estimated by robustly fitting Tx-Rx direct-wave distances to arrival times and applied to synthetic-aperture delay-and-sum reconstruction. We evaluated a geometric phantom, two bone-soft-tissue phantoms, and two human forearms. At the estimated speed of 1507.2 m/s, mean contrast-to-noise ratio (CNR) increased by 8.9% and 11.0%, and geometric bias decreased by 54.5% and 65.1% relative to 1480 and 1540 m/s, respectively. The system visualized bone-mimicking interfaces and produced complete in vivo forearm cross sections, demonstrating the feasibility of reproducible full-circumference musculoskeletal USCT.

Keywords: ring-array ultrasound; ultrasound computed tomography; musculoskeletal imaging; sound-speed calibration; synthetic-aperture imaging

Academic Editors: Lin Huang and Simon Kwoon-ho Chow

Received: 12 September 2026
Revised: 1 November 2026
Accepted: 23 November 2026
Published: 25 November 2026

Copyright: © 2026 by the authors. Licensee MDPI, Basel, Switzerland. This article is an open access article distributed under the terms and conditions of the Creative Commons Attribution (CC BY) license.

1. Introduction

Musculoskeletal ultrasound is widely used to evaluate muscles, tendons, ligaments, nerves, and cortical bone surfaces because it is free of ionizing radiation, enables real-time dynamic assessment, and is readily available at the point of care [1]. Current clinical ultrasound systems rely primarily on handheld linear transducers and provide localized, single-sided two-dimensional views. The quality of handheld ultrasound examinations is highly operator-dependent because probe position, beam incidence angle, acoustic-window selection, and contact pressure vary with operator technique, potentially leading to interoperator variability and reduced longitudinal reproducibility. For limb imaging,

where subcutaneous fat, multiple muscle groups, fascial septa, and bone form a complex cross-section, a single-sided acquisition cannot cover the entire region within a single scan. This limited coverage also constrains standardized measurements of cross-sectional area, tissue boundaries, and structural changes. An ultrasound system with fixed geometry and repeatable data acquisition is therefore needed for quantitative and standardized musculoskeletal assessment.

Freehand three-dimensional ultrasound extends the spatial coverage of conventional two-dimensional imaging by combining spatial tracking with volumetric reconstruction and has been used to measure muscle volume and morphology [2]. However, it still depends on expert scanning technique, remains predominantly a single-sided approach in musculoskeletal applications, and has not been widely adopted in routine clinical practice. This approach generally requires probe calibration, temporal synchronization, registration of irregularly spaced slices, and resampling [3]. Probe contact pressure may also deform local soft tissues and bias estimates of surface contours and tissue volumes [4]. Although freehand three-dimensional ultrasound has demonstrated good measurement reliability [5,6], its reconstructed geometry remains dependent on the scan trajectory and tracking accuracy. By contrast, fixing the transducer around the target and mechanically acquiring regularly spaced cross sections establishes a unified and traceable coordinate system during acquisition, providing a more stable basis for three-dimensional reconstruction.

Ultrasound computed tomography places transmitting and receiving transducers around a target to acquire reflection, scattering, or transmission signals from multiple directions, providing a practical route to complete cross-sectional ultrasound imaging. With fixed acquisition geometry and automated scanning, USCT can reduce dependence on operator-controlled probe motion and provide repeatable cross-sectional coverage. Acquiring and modeling different wave types also enables complementary structural and quantitative acoustic-parameter imaging, while mechanical axial scanning extends two-dimensional cross sections into three-dimensional volumes. As a representative application, breast USCT has achieved promising results through circumferential water-coupled acquisition with fixed geometry and automated scanning [7,8]. It has also advanced quantitative methods such as sound-speed imaging and full-waveform inversion [9,10]. Most USCT systems use circular ring arrays to surround the target. In reflection-mode ring-array USCT, the circular aperture provides full-circumference observations and repeated measurements across transmit positions and receive directions. For reflection imaging with such an array, synthetic-aperture reconstruction coherently combines multi-angle measurements to improve localization and spatial resolution. Ring arrays have enabled high-resolution reflection imaging [11], and studies of capacitive micromachined ultrasonic transducer rings, ring-array plane-wave imaging, and multielement synthetic apertures have demonstrated advantages in dynamic focusing, angular compounding, and effective-aperture extension [12–14].

The application of ring-array USCT to musculoskeletal imaging is not a straightforward transfer of breast-oriented system designs. Unlike the predominantly soft-tissue breast, a limb contains soft tissue and bone with markedly different acoustic properties. Cortical bone has high acoustic impedance and produces strong specular reflections; its attenuation and sound speed also differ substantially from those of surrounding tissues. Consequently, the pronounced acoustic heterogeneity of musculoskeletal tissues, particularly the large sound-speed differences involving bone, poses a major challenge to the homogeneous fixed-sound-speed assumption and can cause travel-time errors, defocusing, and localization bias. Previous studies have compared ray-based, diffraction-corrected, and full-wave models in complex media [15]. Average sound speed has also been estimated from channel coherence or interelement phase variance [16–18], but these

approaches typically require repeated reconstructions over candidate speeds. For cortical-bone imaging, predicted velocity models and full-waveform inversion have improved recovery of the bone-soft-tissue interface [19,20], although their modeling and computational requirements are greater than those of conventional beamforming. These findings indicate an algorithmic need for practical, dataset-specific propagation-time correction in heterogeneous bone-soft-tissue media [21,22].

Ring-array ultrasound tomography systems have recently been explored for limb and human-scale imaging. Li et al. developed an adjustable-radius ring array for three-dimensional imaging of large targets [23]. Hou et al. investigated mechanical slice-by-slice scanning and global sound-speed optimization for three-dimensional reflection imaging with a fixed ring array [24], whereas Zuo et al. improved reconstruction efficiency using multiple subapertures and frequency-domain synthetic-aperture imaging [25]. Garrett et al. used a 512-element circular receive array for cross-sectional tomography of the human body [26–28]. These studies have advanced adaptable apertures, human-scale imaging, mechanically scanned volumetric acquisition, and rapid reconstruction. However, few studies have integrated fixed-geometry, mechanically registered three-dimensional acquisition with sound-speed correction derived directly from the same complete Tx-Rx dataset for musculoskeletal reflection imaging [29–31].

The assumed sound speed determines the transmit-pixel-receive travel time used in synthetic-aperture delay-and-sum (SA-DAS) beamforming. Ring-array Tx-Rx pairs span different distances and viewing directions. When the assumed speed differs from the medium's effective propagation speed, path-dependent timing errors accumulate during coherent summation, causing phase misalignment, main-lobe broadening, elevated sidelobes, and localization errors. In element-wise transmission with multiplexed multichannel reception, Tx-Rx direct waves encode both known geometric distances and measured arrival times. Robust fitting across multiple directions and path lengths can therefore yield a dataset-specific global effective sound speed for subsequent SA-DAS delay correction. Because the direct waves are contained in the same acquisition, this strategy provides practical propagation-time calibration without requiring a separate sound-speed scan.

To address these algorithmic and system-level gaps, this study presents a ring-array system and associated methods for reflection tomography of limb musculoskeletal tissues. The system uses a fixed 512-element ring array with an approximately 100 mm diameter. Sequential element transmission and multiplexed reception are implemented using 128-channel parallel transmit/receive hardware and a transducer switching matrix, providing receive coverage of up to 512 elements for each active transmitter. Mechanical axial scanning supplies regularly spaced cross-sectional datasets for three-dimensional reconstruction. We also propose a global effective sound-speed estimator based on Tx-Rx direct-wave distances and arrival times. Robust regression yields a dataset-specific propagation calibration that corrects transmit-pixel-receive delays in SA-DAS. A geometric reference phantom, two bone-soft-tissue phantoms, and human forearms were used to evaluate sound-speed calibration, structural recovery, target visualization, and three-dimensional continuity.

2. Materials and Methods

2.1. Synthetic-Aperture Delay-and-Sum Beamforming in USCT

This study uses reflection-mode synthetic-aperture acquisition with element-wise transmission and full-array reception. During the mth transmit event, the mth array element emits an ultrasonic pulse, and all array elements synchronously record echoes from tissue interfaces, yielding full-array RF data for that event. This scheme exploits the ring array's full-circumference coverage and provides multi-angle data for subsequent synthetic-aperture reconstruction.

https://doi.org/10.3390/bioengineering13121440

In practical reflection imaging, however, reconstruction need not use every receive channel. To balance image quality and computational efficiency, effective receive elements near the transmitter are selected from the full-array dataset to form a limited receive aperture. This strategy reduces the computational cost per reconstruction and increases the achievable frame rate during continuous scanning while retaining the dominant reflection information. Figure 1 illustrates the imaging configuration. The blue elements denote the receive aperture used to reconstruct the current pixel; they are not the only channels activated during acquisition.

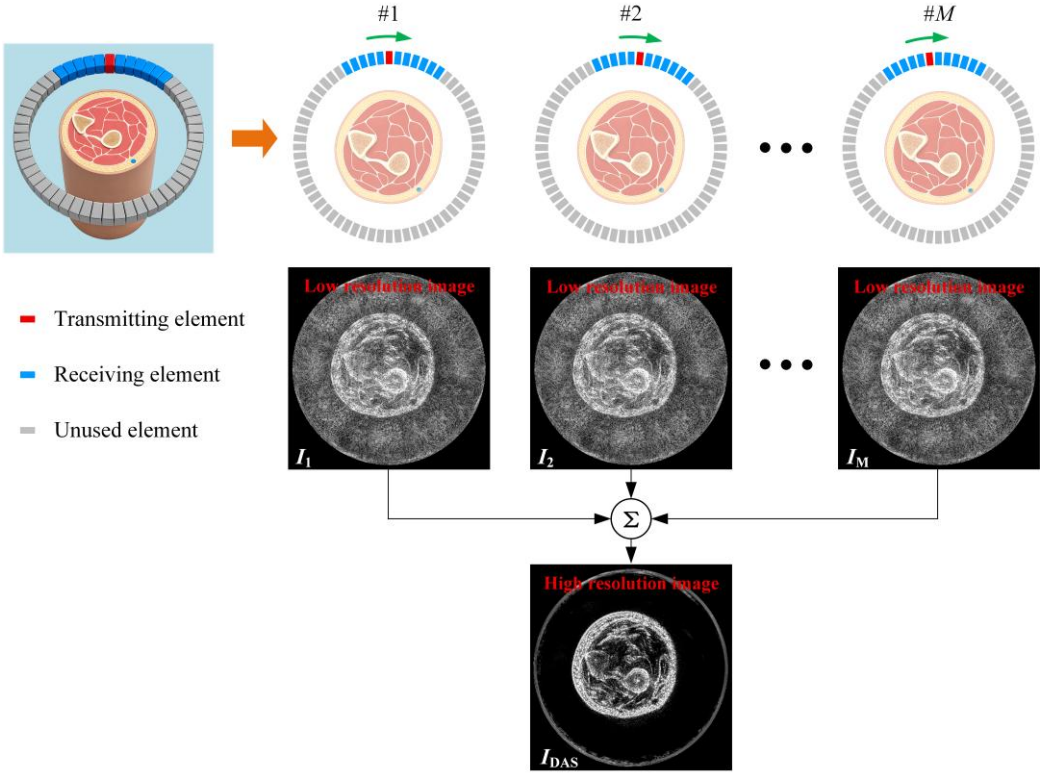


Figure 1. Schematic of synthetic-aperture imaging with the USCT system.

For the mth transmitting element and the nth effective receiving element, their positions are denoted by $\left(x_{t_m}, y_{t_m}\right)$ and $\left(x_{r_n}, y_{r_n}\right)$, respectively, and the image point is denoted by $\left(x, y\right)$. Assuming a homogeneous sound speed c within the tissue, the total transmit-pixel-receive travel time of the reflected wave is given by

$$\tau_{mn}(x,y) = \frac{\sqrt{\left(x-x_{t_m}\right)^2+\left(y-y_{t_m}\right)^2}+\sqrt{\left(x-x_{r_n}\right)^2+\left(y-y_{r_n}\right)^2}}{c} \quad (1)$$

The first and second terms represent the transmit and receive path travel times, respectively.

After RF preprocessing, the complex echo value at each image point is sampled from the corresponding channel using the calculated propagation delay. The low-resolution reflection image for the mth transmit event is

$$I_m(x,y) = \sum_{n\in\Omega_m} w_{mn}(x,y)s_{mn}\left[\tau_{mn}(x,y)\right] \quad (2)$$

where Ω_m denotes the set of effective receiving elements associated with the *m*th transmitting element; $s_{mn}(t)$ denotes the analytic RF signal received by the *n*th array element when the *m*th element transmits; and $w_{mn}(x,y)$ is a weighting function that accounts for element directivity, receive angle, and variations in effective sampling coverage.

Because each transmit event uses a limited receive aperture, its reflection image has relatively low spatial resolution. Sequential activation of different transmit elements produces low-resolution images under different observation geometries:

$$I_1(x,y), I_2(x,y), \ldots, I_M(x,y) \tag{3}$$

Finally, the low-resolution images from all transmit events are coherently summed in the complex domain:

$$I_{DAS}(x,y) = \sum_{m=1}^{M} I_m(x,y) \tag{4}$$

where *M* denotes the number of transmitting elements used in the synthetic-aperture reconstruction.

Coherent integration of reflections from multiple transmit positions enlarges the effective aperture and extends spatial-frequency coverage, thereby improving the localization of tissue interfaces and scatterers in ring-array reflection imaging.

2.2. Global Effective Sound-Speed Estimation

Sound speed is a critical determinant of DAS delay accuracy. To account for the diverse path lengths in a ring array, we estimate a dataset-specific global effective sound speed from Tx-Rx direct waves. Unlike methods that select the sound speed by searching reconstructed-image quality, the proposed approach establishes a distance-time constraint directly from the acquired propagation data. As shown in Figure 2, let the chord length between the *t*th transmit element and the *r*th receive element be:

$$d_{tr} = \sqrt{\left(x_t - x_r\right)^2 + \left(y_t - y_r\right)^2} \tag{5}$$

With the transmit trigger defined as time zero, the direct-wave arrival time T_{tr} approximately satisfies

$$T_{tr} = \frac{d_{tr}}{c} \tag{6}$$

A direct-wave search window is first defined from the Tx-Rx chord distance and an initial sound-speed estimate. The recorded sample time of the dominant analytic-signal envelope peak within this window, referenced to the transmit trigger, defines the measured direct-wave arrival. The detailed channel-selection procedure, search-window settings, and measured RF example are provided in the Supplementary Materials (Section S1 and Figure S1). Valid Tx-Rx measurements spanning multiple azimuths and chord lengths are then fitted by robust regression:

$$\hat{c} = \arg\min_{c} \sum_{(t,r)\in\Omega} w_{tr} \left(T_{tr} - \frac{d_{tr}}{c} \right)^2 \tag{7}$$

where Ω is the set of valid channels used for estimation, w_{tr} is the robust weight iteratively updated from the fitting residuals, and $\hat{c}$ is the global effective sound speed to be estimated.

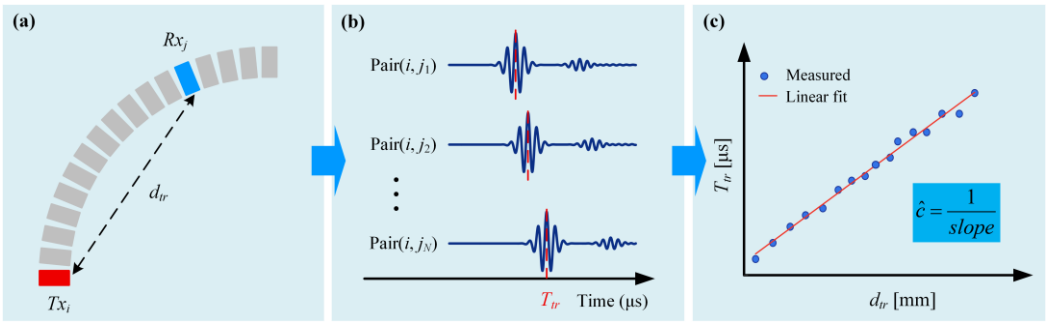


Figure 2. Schematic of global effective sound-speed estimation from Tx-Rx direct waves: (**a**) Tx-Rx chord-path geometry; (**b**) extraction of the direct-wave envelope-peak arrival time; and (**c**) robust global sound-speed regression.

Receive channels with short Tx-Rx separations are excluded because they are susceptible to transmit ringing and electrical coupling. Valid paired measurements sampled from the remaining channels form Ω in Equation (7); measurements with larger fitting residuals receive smaller robust weights. The estimated sound speed $\hat{c}$ is then used to recalculate all transmit-receive path times. This value is a dataset-specific global effective sound speed, not a spatially varying local sound-speed map.

2.3. Three-Dimensional Volume Reconstruction

Three-dimensional data are acquired by mechanical slice-by-slice scanning. At each axial position, the system records RF data using element-wise transmission and multiplexed reception; the corresponding two-dimensional cross section in the x-y plane is subsequently reconstructed using the SA-DAS method described above. The stage then advances to the next prescribed position and repeats the acquisition. Because all slices share the same in-plane coordinate system, they can be ordered along z according to the recorded stage positions to form a three-dimensional ultrasound volume.

Let z_0 denote the initial position of the mechanical scan and Δz the axial step size between adjacent slices. Given a total of K acquired two-dimensional slices, the axial coordinate of the kth slice can be expressed as

$$z_k = z_0 + (k-1)\Delta z, \quad k = 1, 2, \ldots, K \tag{8}$$

Let $I_{DAS}^{(k)}(x, y)$ denote the two-dimensional linear-amplitude image acquired at the kth scanning position. The discrete three-dimensional volume is then defined as

$$V(x, y, z_k) = I_{DAS,}^{(k)}(x, y) \tag{9}$$

All slices are reconstructed with the same array-geometry model, imaging grid, and global effective sound speed to maintain consistent spatial and amplitude scales. This prevents slice-dependent scale changes and misregistration, allowing the linear-amplitude images to be stacked reliably in a common coordinate system.

The mechanical step size typically makes the native axial sampling interval larger than the in-plane pixel spacing, so direct stacking may produce visible interslice discontinuities. We therefore resample the linear-amplitude data along the axial z direction at each fixed in-plane position (x,y). The resulting interpolated volume is expressed as

$$\tilde{V}(x, y, \tilde{z}) = \mathcal{P}_z\{V(x, y, z_k)\} \tag{10}$$

where $\mathcal{P}_z\{\cdot\}$ denotes the interpolation operator along the z direction, and $\tilde{z}$ represents the regularly spaced axial coordinates after resampling. Shape-preserving piecewise cubic

Hermite interpolation is employed to improve interslice continuity while suppressing the local overshoots and spurious extrema that may be introduced by conventional cubic-spline interpolation. The interpolation is performed in the linear-amplitude domain to avoid distortion of the relative amplitude relationships caused by directly interpolating nonlinearly log-compressed images.

3. USCT Imaging System

3.1. System Overview and Workflow

We designed and constructed a ring-array USCT system for reflection tomography of musculoskeletal tissues. The system comprises a scanning chamber, ring-array transducer, multichannel transmit/receive and switching electronics, control cabinet, axial motion stage, and data-processing workstation. The chamber provides a stable water-coupled acoustic environment, and an adjustable support keeps the target within the effective aperture. The fixed ring array provides 360° coverage, while the axial stage acquires consecutive cross sections. The control cabinet supplies power and manages motion and system state; the workstation configures acquisition, transfers data, reconstructs two-dimensional images, and visualizes three-dimensional volumes.

Mechanical positioning defines the spatial reference for acquisition. As shown in Figure 3, the workflow comprises ultrasound transmission/reception, signal acquisition, and image reconstruction. Before scanning, the workstation sets the mechanical origin and scan range; configures excitation voltage, pulse cycles, sampling frequency, record length, and receive gain; and loads the element coordinates and transmit sequence. After target fixation, the stage moves to the first slice position, where sequential element excitation and full-array reception are performed. The indexed RF data are transferred to the workstation for cross-sectional reconstruction and subsequent volume assembly.

For each cross section, the transmit element remains fixed while the switching matrix sequentially connects different receive groups. Each group is synchronously sampled, and the data are concatenated by global element index to provide signals from up to 512 receive elements per transmit event. Repeating this process for all 512 transmit elements yields an RF dataset with dimensions of time samples × receive elements × transmit elements. This architecture enables complete circular-aperture acquisition using only 128 parallel hardware channels.

Each frame stores the transmit index, receive group, mechanical position, sampling parameters, and timestamp so that data from different boards, receive groups, and axial slices can be assembled correctly. After the current slice has been processed or stored, the stage advances by the prescribed step and repeats the acquisition until the axial range is covered.

A common clock and unified timing controller synchronize transmission, reception, and data transfer. Recording the stage position and channel indices allows all cross sections to be reconstructed in a common spatial coordinate system.

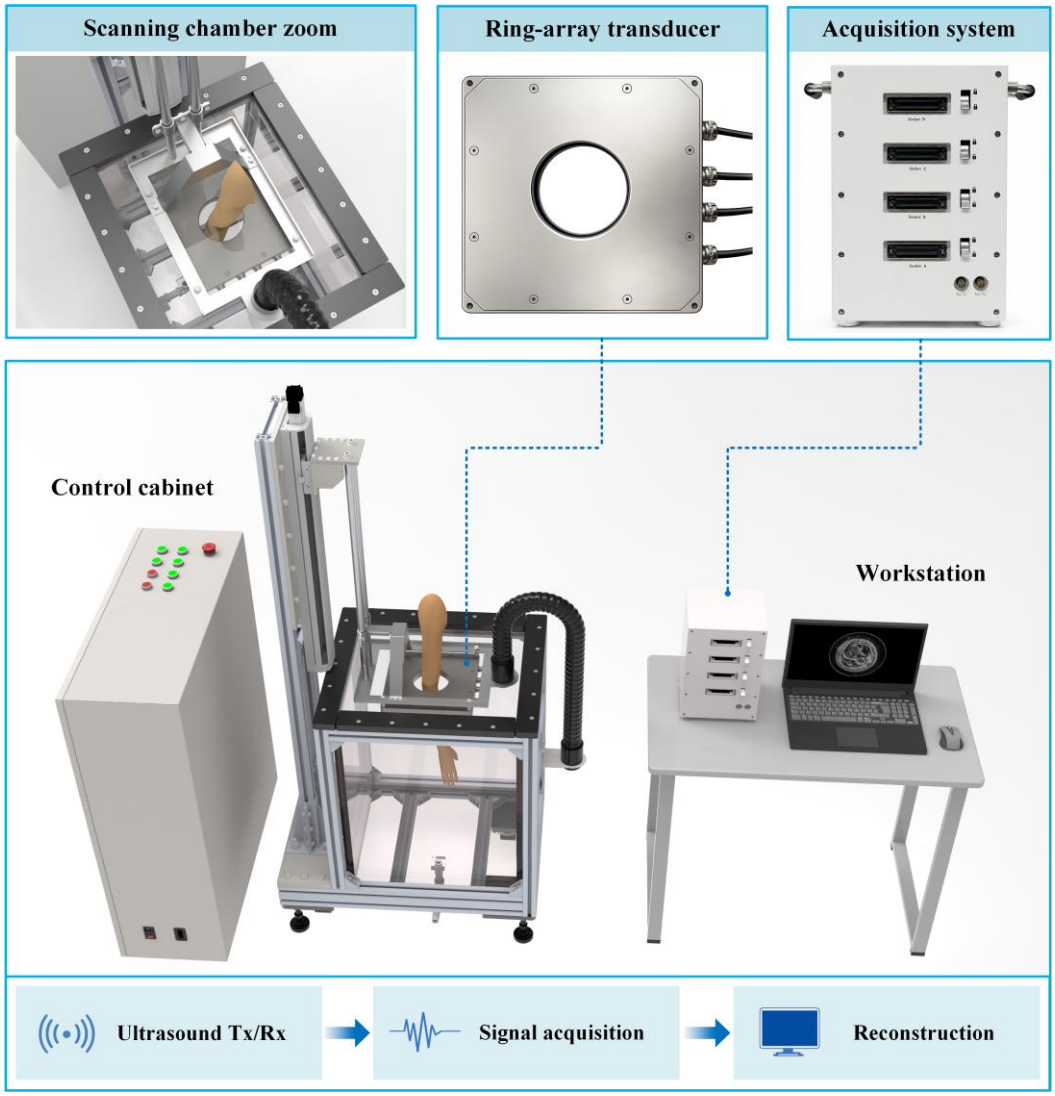


Figure 3. System configuration and acquisition-to-reconstruction workflow of the ring-array USCT platform.

3.2. Multichannel Transmit/Receive Electronics

Figure 4 presents the multichannel ultrasound transmit/receive architecture used for sequential element excitation, parallel echo acquisition, synchronized board operation, and PCIe data transfer. The system comprises a host computer (Host PC), PCIe switch, two 64-channel transmit/receive boards (Boards 1 and 2), a board-to-board synchronization link, a transducer switching matrix, and four transducer interfaces (Slots A–D). The Host PC configures the acquisition sequence, receives and stores raw RF data, and performs offline reconstruction, while the PCIe switch distributes control commands and aggregates data from both boards. Together, the two boards provide 128 parallel receive channels, which the switching matrix sequentially connects to four non-overlapping groups of 128 elements within the 512-element ring array. In full-matrix mode, each transmitting element is excited four times, with a different receive group connected before each excitation. The 128 connected channels synchronously record RF signals over the complete acquisition window, and the four group records are assembled according to global receive-element indices to obtain 512 receive traces for that transmitter. Repeating this sequence for all 512 transmitting elements requires 2048 physical transmit events per cross section and produces a dataset with dimensions of time samples × 512 receiving elements × 512 transmitting elements.

As shown in Figure 4, an FPGA coordinates the operation of each transmit/receive board. Dedicated clock and synchronization circuits establish a common timing reference within and between the boards, aligning transmit triggers, sampling clocks, and frame indices. Separate power-management domains supply the digital-control, high-voltage transmit, and analog receive circuits to reduce noise coupling. The FPGA trigger-management block schedules excitation and sampling, while the TGC-control block applies time-dependent receive gain.

Each transceiver board integrates four 16-channel analog front-end (AFE) modules and four 16-channel high-voltage pulser modules, which are connected to the external transducer switching matrix through a 64-channel connector. Before acquisition, the Host PC sends the transmit-element index, receive configuration, excitation parameters, TGC curve, and record length to the boards. After interboard synchronization, the FPGA programs the selected pulser according to the prescribed channel-enable signals, pulse width, cycle count, and interelement delay, while the switching matrix routes the electronic channels to the designated transducer slot or element group. After the transmit-protection interval, the AFE performs low-noise amplification, time-gain adjustment, bandwidth limiting, and analog-to-digital conversion. The FPGA then maps the channel indices, organizes the frame metadata, and converts the data format. Repeating this sequence across transmit elements produces single-transmit, multireceive RF data for synthetic-aperture imaging.

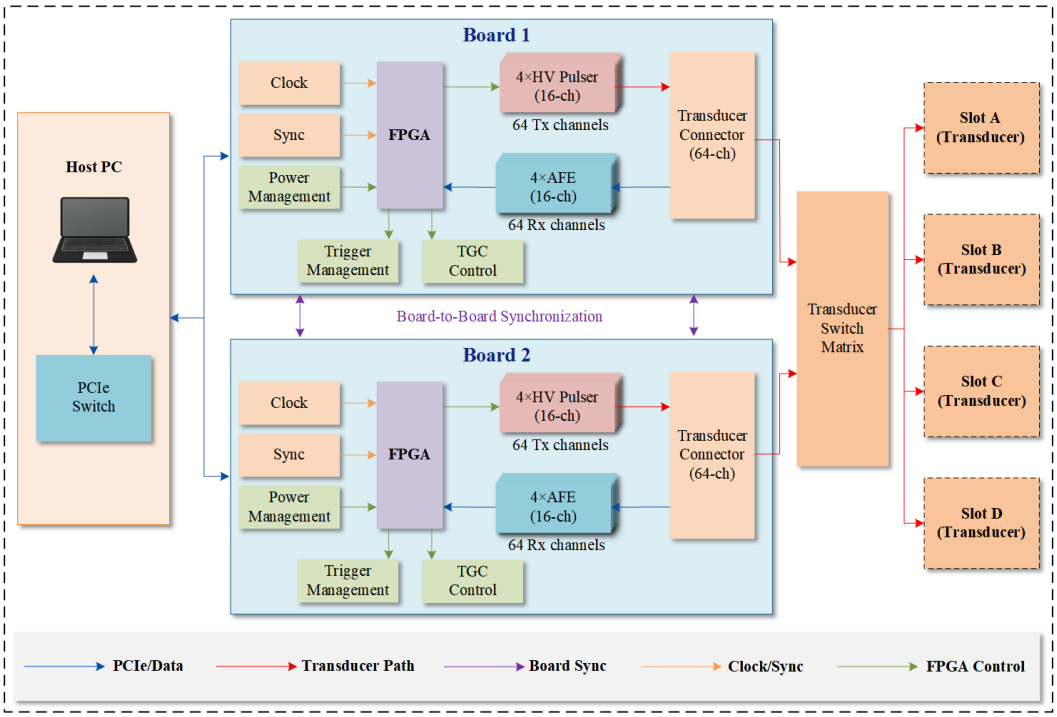


Figure 4. Block diagram of the multichannel ultrasound transmit/receive electronics.

Ring-array acquisition generates large multichannel RF datasets. The two boards therefore transfer data through the PCIe switch and Thunderbolt interface to the Host PC, where the RF records are indexed, stored, and prepared for offline reconstruction. This high-throughput data link reduces transfer bottlenecks and supports subsequent beamforming and volume reconstruction. Under the experimental conditions used in this study, the system can achieve an acquisition rate of up to 8 frames/s.

The board-to-board synchronization link places data from both boards on a common time axis, while the switching matrix maps the 128 electronic channels to designated

transducer slots or element groups. This modular interface supports different probe configurations and acquisition modes without redesigning the core electronics.

3.3. Ring-Array Transducer

The transducer is a single-ring array of 512 elements uniformly distributed on a 50 mm-radius circle with a 0.62 mm center-to-center pitch, providing 360° acquisition. Its center frequency is 3 MHz, the −6 dB fractional bandwidth is approximately 75%, and the −20 dB single-pulse duration is no greater than 1.35 μs. During each two-dimensional acquisition, elements are sequentially activated as transmitters, while the switching matrix connects the configured receive groups to the 128-channel electronics. Depending on the acquisition configuration, RF signals from up to 512 receive elements can be assembled for each active transmitter. The sampling frequency is configurable from 12.5 to 50 MHz to accommodate different imaging depths and resolution requirements. Table 1 summarizes the principal specifications.

Table 1. Ring-array transducer specifications.

Parameter	Value
Number of elements	512
Center frequency	3 MHz ± 10%
Fractional bandwidth (−6 dB)	75%
Array radius	50 mm
Element center spacing	0.62 mm
Sampling rate	12.5–50 MHz
Pulse duration (−20 dB)	≤1.35 μs

4. Experimental Methods

The experimental program comprised a geometric reference phantom, two bone–soft-tissue phantoms, in vivo forearm imaging, and mechanical three-dimensional scanning. These experiments evaluated geometric accuracy, target contrast, and structural visibility, in vivo feasibility, and three-dimensional spatial consistency. Except in the sound-speed comparison, acquisition and reconstruction settings were held constant within each experiment.

4.1. Phantom Design

A geometric reference phantom and two bone-soft-tissue phantoms were used to evaluate the ring-array USCT system under different acoustic conditions. The geometric phantom tested spatial localization and sound-speed calibration, whereas the bone-soft-tissue phantoms assessed structural visibility in the presence of strongly reflecting interfaces and different scattering backgrounds.

The geometric reference phantom was a 58 mm-diameter cylinder. Its cross section contained two circular high-sound-speed inclusions, each 12 mm in diameter and separated by 28 mm center-to-center (Figure 5). This regular geometry provided a spatial reference for quantitative assessment of target-size recovery and localization accuracy.

The background and inclusions were fabricated from agar-glycerol matrices containing quartz sand as the scattering component. Acoustic contrast was produced by varying the material composition. The mass ratios of agar, glycerol, quartz sand, and water were 4:7:1:100 in the background and 4:10:1:100 in the high-sound-speed inclusions.

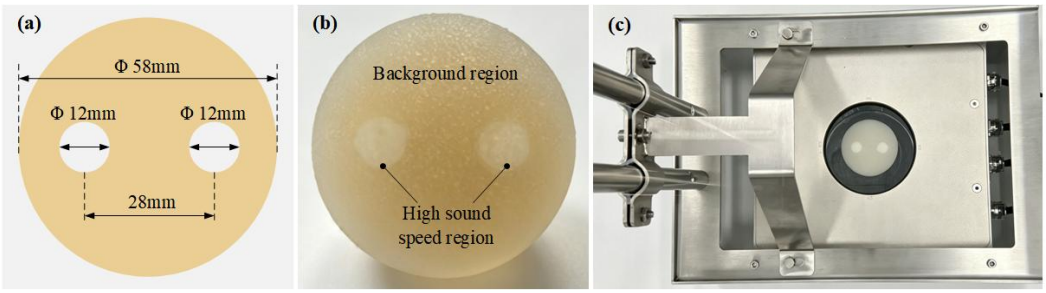


Figure 5. Geometric reference phantom used for system validation: (**a**) nominal cross-sectional geometry; (**b**) fabricated phantom; and (**c**) phantom positioned within the ring-array imaging aperture.

The bone-soft-tissue phantoms shared the same cross-sectional geometry so that the bone-mimicking contours, positions, and orientations were consistent. As shown in Figure 6, Phantom A contained a 3D-printed resin bone-mimicking structure within an agar-glycerol-water matrix without quartz sand (mass ratio, 4:7:100). Phantom B contained a 3D-printed polylactic acid (PLA) bone-mimicking structure within an agar–glycerol-quartz sand-water matrix (4:7:0.5:100). The phantoms therefore represented strongly reflecting bone-mimicking structures in low-scattering and scatterer-containing backgrounds, respectively. The two phantoms provided complementary imaging scenarios for assessing structural visibility under different acoustic conditions. Because the bone-mimicking material and background scattering varied together, the comparison does not isolate the individual contribution of either factor.

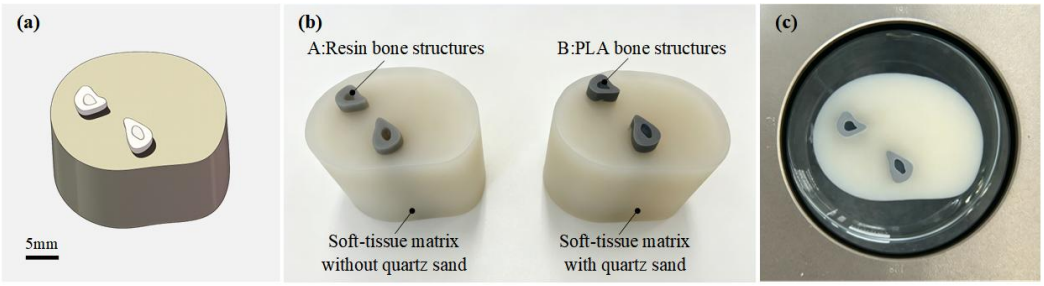


Figure 6. Bone-soft-tissue composite phantoms: (**a**) common structural model; (**b**) fabricated phantoms with resin (A) and PLA (B) bone-mimicking structures; and (**c**) water-coupled experimental configuration.

4.2. Experimental Setup

All phantom experiments were conducted under water-coupled conditions, with the ring array fixed inside the imaging chamber and each phantom positioned within the effective imaging region of the array. For each cross section, all 512 elements were sequentially activated as individual transmitters, and the RF echo data from the corresponding receive elements were recorded for each transmit event. Sixteen axial slices of the geometric reference phantom were acquired at intervals of 1 mm. Phantoms A and B were scanned over 20 and 15 axial slices, respectively, with the same 1 mm spacing. Identical acquisition and reconstruction settings were applied to all phantom experiments to ensure comparability among the resulting images.

For in vivo imaging, the forearm was scanned while the participant remained relaxed. To accelerate acquisition and reconstruction, the effective receive aperture was limited to 128 elements, with one transmit event per element. All RF datasets were reconstructed using the global sound-speed estimator and SA-DAS method described above.

In the sound-speed comparison, only the propagation speed used for reconstruction was varied; all other parameters were unchanged.

For three-dimensional visualization, reconstructed slices were positioned according to the recorded mechanical displacements in a common coordinate system. The discrete axial samples were then resampled by shape-preserving piecewise cubic Hermite interpolation (PCHIP) to improve interslice display continuity.

4.3. Quantitative Evaluation

Quantitative evaluation focused on target-background distinguishability and geometric recovery. All intensity-based metrics were calculated from linear-envelope images before logarithmic compression to avoid bias from the nonlinear display transform.

Target-background distinguishability was quantified by the contrast-to-noise ratio (CNR). Circular regions of interest (ROIs) were selected in each target and an adjacent background region. Pixels from both target ROIs were pooled for target statistics, and CNR was defined as

$$\mathrm{CNR} = \frac{\left|\mu_{\mathrm{tar}} - \mu_{\mathrm{bg}}\right|}{\sqrt{\sigma_{\mathrm{tar}}^2 + \sigma_{\mathrm{bg}}^2}} \tag{11}$$

where μ_{tar} and μ_{bg} denote the mean envelope amplitudes within the target and background regions, respectively, σ_{tar} and σ_{bg} denote the corresponding standard deviations. A larger CNR indicates better target-background contrast.

Geometric measurement accuracy was evaluated using percentage bias (Bias):

$$\mathrm{Bias} = \frac{\left|L_{\mathrm{rec}} - L_{\mathrm{ref}}\right|}{L_{\mathrm{ref}}} \times 100\% \tag{12}$$

where L_{rec} denotes the geometric dimension measured from the reconstructed image, and L_{ref} denotes the corresponding design value. For each reconstructed image, Bias was calculated as the arithmetic mean of the absolute percentage errors of all reference dimensions (the 58 mm outer diameter, both 12 mm inclusion diameters, and the 28 mm center-to-center spacing). Bias was calculated separately for each image.

CNR and Bias quantify complementary aspects of performance: image contrast and geometric accuracy, respectively. Together, they address the primary evaluation objectives without duplicating the same image property.

5. Results

5.1. Geometric Reference Phantom

Figure 7 relates the Tx-Rx direct-wave propagation distance to arrival time in the geometric reference phantom. Valid measurements obtained across different transmit azimuths and chord lengths follow an approximately linear trend, indicating that direct-wave arrival time reliably reflects path length and supports geometry-constrained estimation of the global effective sound speed. Each colored marker represents a valid Tx-Rx measurement from the same dataset, and its color denotes the final robust-regression weight w_{tr}, as indicated by the color bar. Warmer-colored markers have higher weights and contribute more strongly to the fit, whereas cooler-colored markers have lower weights and less influence. This weighting reduces the effects of large-residual measurements caused by arrival-time extraction uncertainty, residual transmit ringing, electrical coupling, or path-dependent acoustic variations. The red line represents the robust

distance-time fit, whose reciprocal slope gives the estimated sound speed. After excluding short-separation channels and applying robust weighted regression, the estimated value was $\hat{c}$ = 1507.2 m/s. Unlike image-quality-based searches, this estimate is derived directly from the physical distance-time relationship and is therefore independent of echo amplitude, display dynamic range, and postprocessing settings. Thus, the direct waves also provide dataset-specific propagation calibration without requiring a separate sound-speed scan. Table 2 summarizes the estimates for all datasets.

The fitted value is a path-averaged calibration parameter rather than a local sound-speed map. Its role in SA-DAS is to place Tx-Rx paths of different lengths and azimuths on a common, dataset-matched time scale, thereby reducing phase dispersion during coherent summation and improving overall focus.

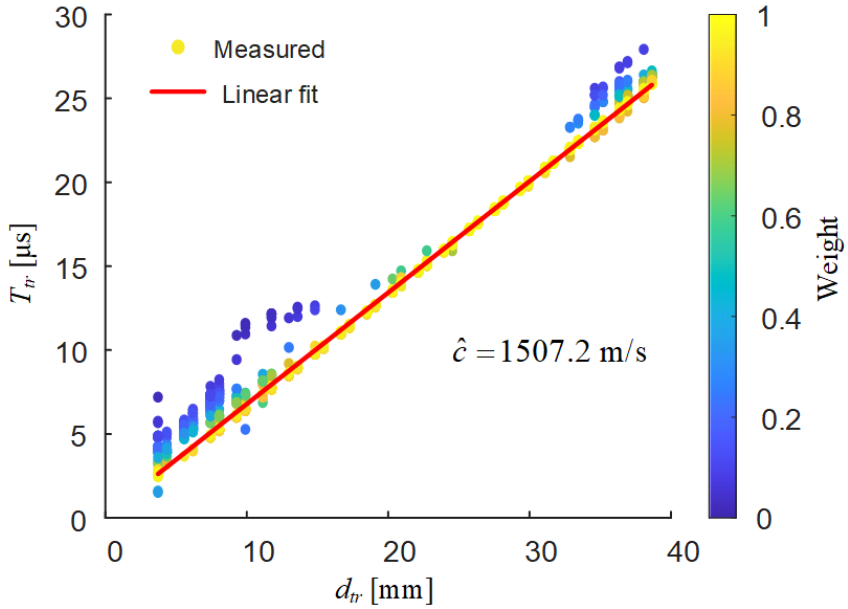


Figure 7. Global effective sound-speed estimate for the geometric reference phantom.

Table 2. Estimated global effective sound speeds used for image reconstruction.

Dataset	Global Effective Sound Speed (m/s)
Geometric reference phantom	1507.2
Bone-soft-tissue Phantom A	1491.3
Bone-soft-tissue Phantom B	1477.5
Male forearm	1496.0
Female forearm	1499.5

To isolate the effect of sound speed, Figure 8 compares reconstructions generated from identical RF data, receive apertures, imaging grids, and display settings using 1480, 1540, and the estimated 1507.2 m/s. As shown in Table 3, 1507.2 m/s yielded a mean CNR of 0.941 across 16 slices, improvements of 8.9% and 11.0% relative to 1480 and 1540 m/s, respectively. Mean geometric Bias decreased to 1.10%, a reduction of 54.5% and 65.1%. The simultaneous gains in CNR and Bias indicate improved temporal alignment rather than simple intensity rescaling: better alignment concentrates coherent echo energy at the correct locations and sharpens target boundaries.

Because each ring-array pixel integrates paths spanning a broad range of lengths and azimuths, a fixed-speed error produces nonuniform arrival-time errors. The direct-wave-derived estimate places these paths on a common data-driven time scale, establishing the

causal sequence from propagation calibration to corrected SA-DAS delays and improved image quality.

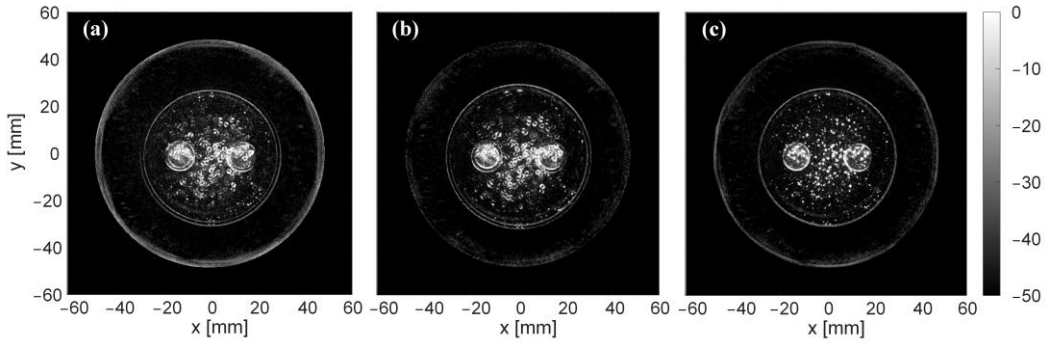


Figure 8. Twodimensional reconstructions of Slice 1 obtained using different sound speeds: (**a**) 1480 m/s; (**b**) 1540 m/s; and (**c**) the estimated sound speed of 1507.2 m/s.

Table 3. Mean image-quality metrics obtained using different reconstruction sound speeds.

Sound Speed (m/s)	CNR	Bias
1480	0.864 ± 0.092	(2.42 ± 0.10) %
1540	0.848 ± 0.104	(3.15 ± 0.11) %
1507.2	0.941 ± 0.084	(1.10 ± 0.08) %

Note: Values are presented as mean ± standard deviation across 16 slices.

Figure 9 evaluates interslice consistency across 16 consecutive axial slices using the estimated sound speed. Both 12 mm targets remained distinguishable in every slice, with little variation in center position, spacing, or contour along z. CNR ranged from 0.806 to 1.065 (mean, 0.941), and geometric Bias ranged from 0.96% to 1.25% (mean, 1.10%), remaining below 1.3% in every slice. The narrow Bias range indicates consistent array geometry, mechanical coordinates, and sound-speed calibration across the scan, without appreciable scale drift.

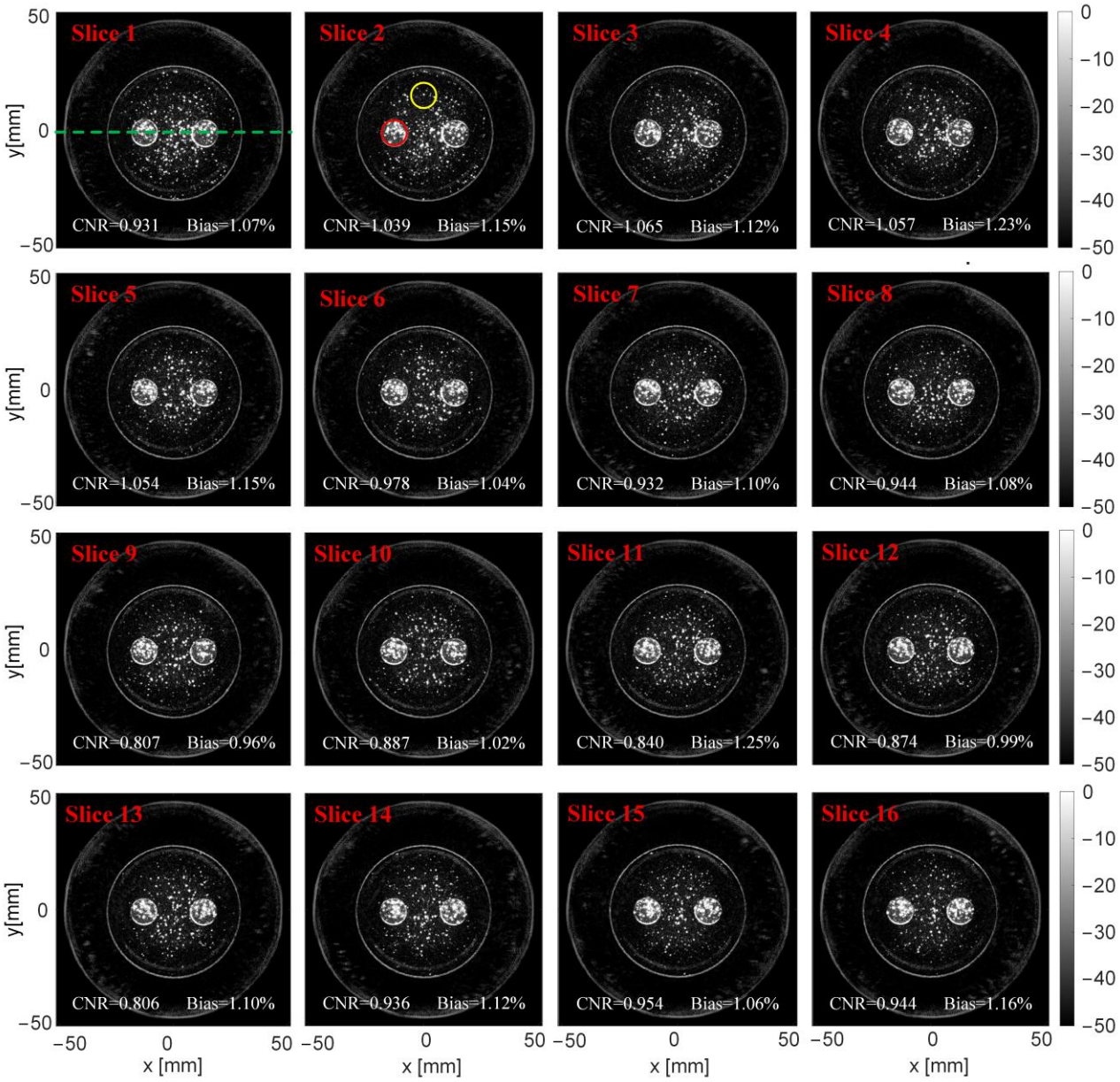


Figure 9. Two-dimensional reconstructions of 16 consecutive axial slices of the geometric reference phantom.

Despite modest CNR fluctuations with local scattering, the stable Bias values show that structural localization is consistent across axial planes. This combination of in-plane accuracy and interslice coordinate consistency is essential for stacking slices without distorting the target trajectory in three dimensions.

Figure 10 shows the lateral amplitude profile of Slice 1 at y = −0.4 mm, a line that intersects both high-sound-speed targets. Each red target interval corresponds to a distinct cluster of high-amplitude responses, whereas the blue regions outside and between the targets remain at lower amplitudes. The return to background level between targets indicates that high-amplitude energy is localized near the nominal target positions rather than distributed nonspecifically across the image. This correspondence supports coherent focusing of the calibrated Tx-Rx echoes at the correct lateral locations.

Image morphology, CNR, Bias, and the lateral profile therefore provide complementary evidence of target visibility, contrast, geometric accuracy, and localization. Together, they show that direct-wave calibration improves ring-array DAS delay matching while

preserving target position and size properties required for consecutive-slice reconstruction and quantitative three-dimensional characterization.

Figure 11 presents the interpolated three-dimensional volume generated from the reconstructed cross-sectional images according to their recorded mechanical z positions. Within the volume, the two circular targets form continuous columnar responses and maintain stable lateral positions along the z direction, while the x-z view shows no obvious global misregistration. These observations confirm that the in-plane ring-array coordinates and mechanical z coordinates are consistently integrated within a common spatial framework. PCHIP interpolation was applied only along the z direction to improve visual continuity between the acquired slices; it neither introduces new axial information nor increases the intrinsic axial resolution. Figure 11 therefore demonstrates interslice registration and spatial coherence of the reconstructed volume rather than an enhancement in axial resolution.

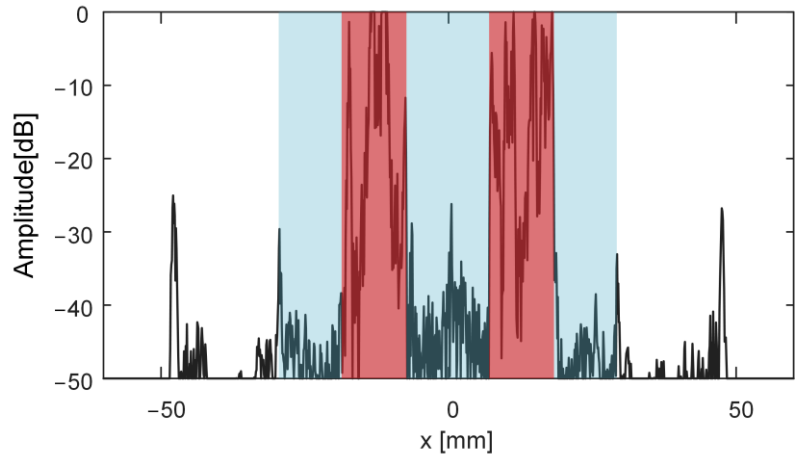


Figure 10. Lateral amplitude profile of Slice 1 at y = −0.4 mm. Red regions indicate the high-sound-speed targets, and blue regions indicate the background.

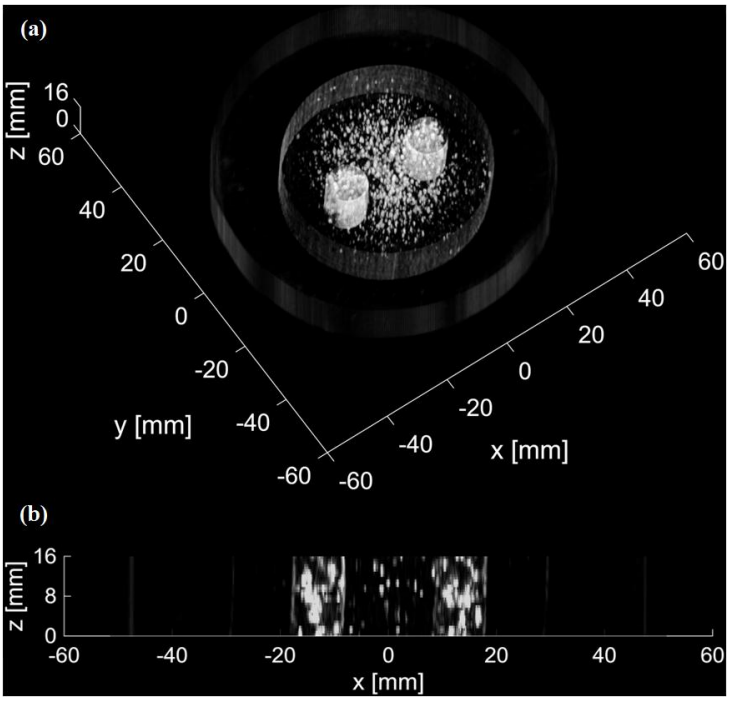


Figure 11. Three-dimensional reconstruction of the geometric reference phantom: (**a**) perspective view; (**b**) x-z view.

5.2. Bone-Soft-Tissue Phantoms

After geometric validation, two bone-soft-tissue phantoms were used to assess strongly reflecting interfaces under different scattering backgrounds. Because resin and PLA have higher sound speeds and attenuation than the surrounding matrices and more closely approximate bone-like acoustic contrast, the analysis focused on interface detectability, contour continuity, and interslice persistence rather than dimensional bias. Estimated global effective sound speeds were 1491.3 m/s for Phantom A and 1477.5 m/s for Phantom B. Figure 12 shows representative slices displayed with the same dynamic range. Additional reconstructions at fixed sound speeds of 1480 and 1540 m/s are provided in Supplementary Section S2.

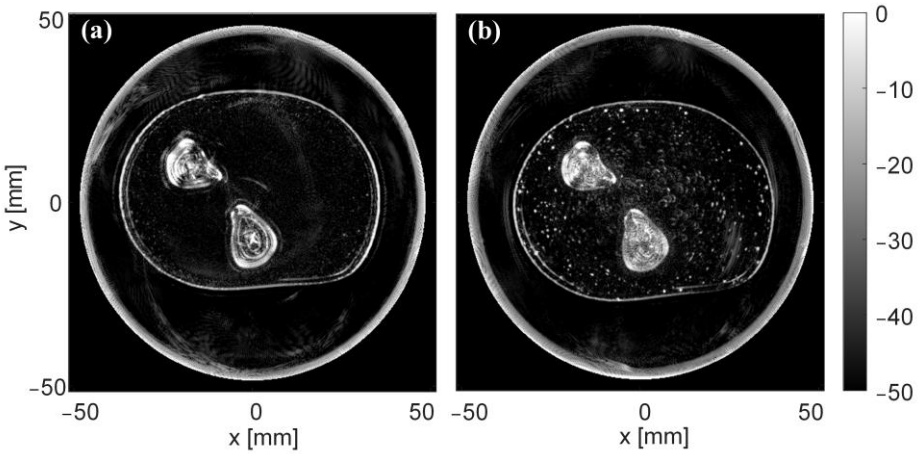


Figure 12. Slice 1 reconstructions of the bone–soft-tissue phantoms: (**a**) Phantom A; (**b**) Phantom B.

In Phantom A, both bone-mimicking structures appear as continuous high-amplitude interfaces whose principal contours are clearly distinguished from the low-scattering background. The large impedance mismatch at the material boundary makes these interfaces the dominant responses. Phantom B exhibited more pronounced background speckle and local amplitude variation, while both bone-mimicking structures remained dominant at their expected positions and their principal boundaries remained visible. Thus, the principal contours were identifiable in both combinations of bone-mimicking material and background.

The visibility of the principal contours in Phantom B supports the feasibility of interface imaging in the tested scatterer-containing configuration. Multi-angle acquisition can provide complementary observations when echoes are weak at individual specular orientations. This setting more closely approximates musculoskeletal tissue, where strong interfaces coexist with diffuse soft-tissue scattering.

Figure 13 provides a qualitative visualization of the axial consistency of the bone-mimicking structures. In Phantom A, both targets remain spatially coherent across consecutive slices and are prominent against the low-scattering background. In Phantom B, volume scattering is more apparent, but the principal structures can still be traced across multiple slices, with relative positions consistent with the two-dimensional images. These observations qualitatively support reflection-based localization and morphological visualization of the bone-like interfaces. However, they do not imply quantitative recovery of the internal bone structure, because impedance mismatch, refraction, sound-speed heterogeneity, and post-bone attenuation still cause information loss.

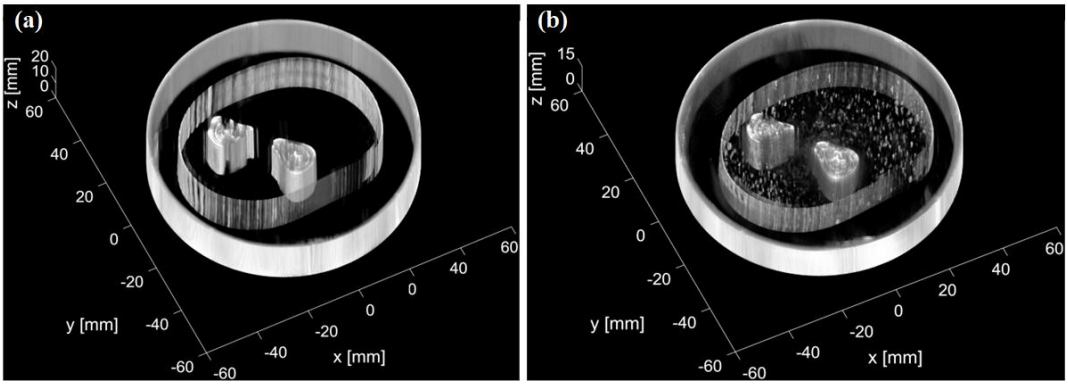


Figure 13. Three-dimensional reconstructions of the bone-soft-tissue phantoms: (**a**) Phantom A; (**b**) Phantom B.

5.3. In Vivo Human Forearm Imaging

Following the phantom studies, human forearms were imaged in vivo using the same fixed-array acquisition, global sound-speed estimation, and SA-DAS workflow. Dataset-specific global effective sound speeds of 1496.0 m/s and 1499.5 m/s were estimated for the male and female forearms, respectively (Table 2). Figure 14 presents representative cross-sectional reconstructions together with an anatomical reference. This experiment assessed whether the complete acquisition and reconstruction workflow could be transferred from controlled phantoms to heterogeneous human tissue while maintaining full-circumference structural visualization. Additional reconstructions at fixed sound speeds of 1480 and 1540 m/s are provided in Supplementary Section S2.

Both in vivo reconstructions delineated the complete outer forearm contour and exhibited spatially organized reflection patterns broadly consistent with the anatomical arrangement shown in Figure 14a. Peripheral echoes were spatially consistent with the skin and subcutaneous fat layers, whereas the interior of the limb showed heterogeneous reflection texture associated with muscular soft tissue. Strong localized responses were observed at the expected positions of the radius and ulna, consistent with the pronounced acoustic-impedance contrast at cortical bone-soft-tissue interfaces. Although the present reflection images do not resolve the internal structure of bone, the simultaneous visualization of the outer contour, soft-tissue texture, and bone-associated interfaces demonstrates that the ring-array system can recover the principal musculoskeletal features across a complete forearm cross section.

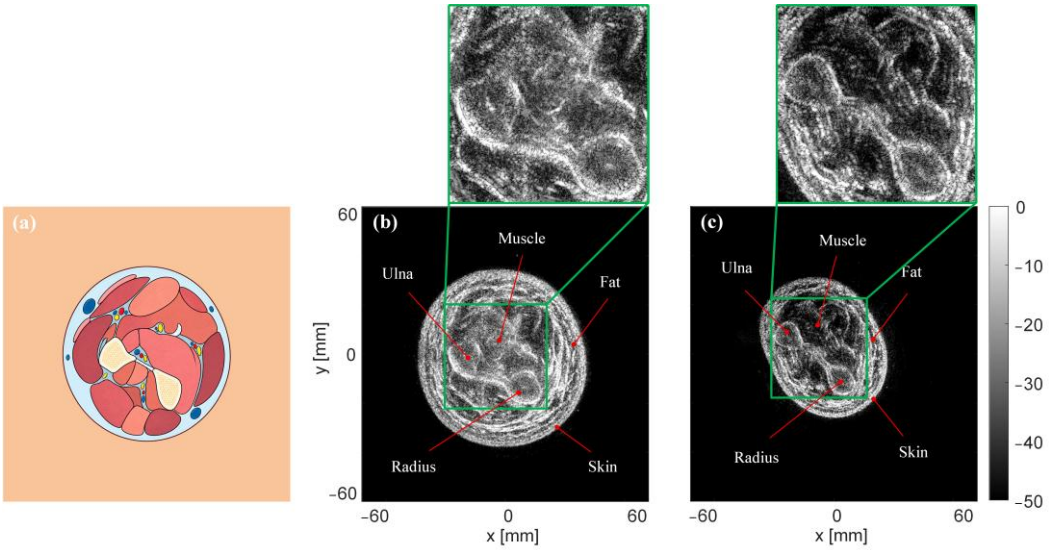


Figure 14. In vivo forearm cross-sectional USCT imaging. (**a**) Anatomical reference of the human forearm cross-section [32]; (**b**) imaging result of a male participant; (**c**) imaging result of a female participant.

Because the final SA-DAS image coherently combines observations from multiple Tx-Rx geometries, the persistence of bone-associated responses at the expected cortical locations is consistent with reduced dependence on a single insonification direction. This characteristic is particularly relevant to bone imaging, where specular reflection strength varies with incidence angle. Together with the phantom results, the in vivo reconstructions show that the same direct-wave sound-speed calibration and synthetic-aperture reconstruction framework remains applicable as acoustic complexity increases from controlled phantoms to heterogeneous human tissue.

Taken together, the in vivo results demonstrate the system-level integration of fixed-geometry acquisition and reconstruction. The ring array provides a consistent circumferential coordinate frame; the switching architecture maintains array-element coverage with 128 parallel hardware channels; Tx-Rx direct waves from the same dataset provide a dataset-specific propagation reference; and calibrated SA-DAS combines the resulting multi-angle echoes into a complete cross-sectional image. Importantly, this workflow achieves these functions without external spatial tracking or a separate sound-speed calibration scan.

6. Discussion

The proposed ring-array USCT system addresses three limitations of handheld musculoskeletal ultrasound: restricted field of view, operator-dependent spatial repeatability, and delay errors caused by sound-speed mismatch. Fixed geometry enables reflection data from multiple directions to be fused in one coordinate system, improving structural localization and complete cross-sectional coverage.

Direct-wave calibration provides the propagation-time reference required for coherent SA-DAS without an additional acquisition. In the geometric phantom, the resulting 1507.2 m/s estimate improved both mean CNR and geometric Bias relative to the two fixed-speed reconstructions. The concurrent improvement in contrast and geometry supports the proposed mechanism: reducing path-dependent timing errors increases coherence and concentrates echo energy at the correct locations.

The calibrated value remains a global effective parameter, not the true local sound-speed distribution. Fat, muscle, and bone differ substantially in acoustic properties, so local speed variation and refraction may still limit quantitative accuracy. Nevertheless, a dataset-matched global reference removes a major systematic error in DAS reflection imaging without increasing acquisition complexity, making it a practical baseline calibration step.

The hardware architecture complements this calibration strategy. A fixed 512-element ring array and switching matrix provide complete circumferential coverage with 128 parallel channels, while axial scanning supplies registered slices for volumetric reconstruction. The phantom and forearm experiments show that this configuration preserves strong interface visibility across scattering conditions and can extend from controlled targets to heterogeneous in vivo anatomy.

Several limitations remain. The homogeneous global-speed model does not account for local sound-speed variation, refraction, or attenuation behind bone. Future work should investigate spatially varying speed models, full-wave propagation compensation, and joint reflection–transmission reconstruction for more quantitative imaging of bone-soft-tissue media. GPU parallelization, higher-throughput data transfer, and accelerated synthetic-aperture algorithms may reduce processing time. Larger in vivo studies are also needed to establish repeatability and clinical utility.

7. Conclusions

We developed a ring-array USCT platform for complete cross-sectional musculoskeletal imaging and a Tx-Rx direct-wave method for global effective sound-speed calibration. The 512-element array, 128-channel electronics, switching matrix, axial scanning, and calibrated SA-DAS workflow enable standardized 360° reflection acquisition and three-dimensional reconstruction. Geometric, bone-soft-tissue, and in vivo forearm experiments demonstrated improved delay consistency, accurate structural recovery, and stable full-circumference imaging. The platform provides a practical basis for standardized extremity imaging and future quantitative and clinical studies. The proposed framework establishes a standardized acquisition and reconstruction basis for future quantitative musculoskeletal ultrasound tomography.

Supplementary Materials: The following supporting information can be downloaded at: https://www.mdpi.com/article/10.3390/bioengineering13121440/s1. The standalone Supplementary Materials file contains details of direct-wave channel selection, search-window settings, and arrival-time extraction with a measured RF example (Section S1 and Figure S1), together with additional reconstructions of the bone-soft-tissue phantoms and human forearms using fixed sound speeds of 1480 and 1540 m/s (Section S2 and Figure S2).

Author Contributions: Conceptualization, C.W. and W.Q.; Methodology, C.W., Z.L., G.Z., and W.Q.; Software, C.W. and Z.L.; Validation, W.F., X.Y., and C.C.; Investigation, C.W., Z.L., W.F., X.Y., and C.C.; Supervision, G.Z., C.C., and W.Q.; Writing-original draft preparation, C.W.; Writing-review and editing, Z.L., W.F., X.Y., C.C., G.Z., L.S., and W.Q. All authors have read and agreed to the published version of the manuscript.

Funding: This research was funded by the Basic Research Program of Jiangsu (Grant No. BK20253037), the Advanced Technology Research and Development Program of Jiangsu (Grant No. BF2025018), and the Pilot Technology Pre-Research Project of the Wuxi Industrial Innovation Research Institute (Project Name: Research on Key Technologies for a Ring-Array Ultrasound Computed Tomography Imaging System).

Institutional Review Board Statement: The study was conducted in accordance with the Declaration of Helsinki and approved by the IEC for Clinical Research of Zhongda Hospital, Affiliated to Southeast University (2017ZDKYSB160).

Informed Consent Statement: Written informed consent to participate in the study and to publish the anonymized ultrasound images was obtained from all participants.

Data Availability Statement: The original contributions presented in this study are included in the article. Further inquiries can be directed to the corresponding authors.

Conflicts of Interest: The authors declare no conflicts of interest.

References

1. Chew, E.; Day, A.L.; Nazarian, L.N.; Kohler, M. Basic Musculoskeletal Ultrasound. *Med. Clin. N. Am.* **2025**, *109*, 137–161.
2. Mozaffari, M.H.; Lee, W.S. Freehand 3-D Ultrasound Imaging: A Systematic Review. *Ultrasound Med. Biol.* **2017**, *43*, 2099–2124.
3. Mercier, L.; Langø, T.; Lindseth, F.; Collins, D.L. A Review of Calibration Techniques for Freehand 3-D Ultrasound Systems. *Ultrasound Med. Biol.* **2005**, *31*, 449–471.
4. Treece, G.M.; Prager, R.W.; Gee, A.H.; Berman, L. Correction of Probe Pressure Artifacts in Freehand 3D Ultrasound. *Med. Image Anal.* **2002**, *6*, 199–214.
5. Cenni, F.; Monari, D.; Desloovere, K.; Aertbeliën, E.; Schless, S.H.; Bruyninckx, H. The Reliability and Validity of a Clinical 3D Freehand Ultrasound System. *Comput. Methods Programs Biomed.* **2016**, *136*, 179–187.
6. Weide, G.; van der Zwaard, S.; Huijing, P.A.; Jaspers, R.T.; Harlaar, J. 3D Ultrasound Imaging: Fast and Cost-Effective Morphometry of Musculoskeletal Tissue. *J. Vis. Exp.* **2017**, *129*, e55943. https://doi.org/10.3791/55943.

7. Duric, N.; Littrup, P.; Babkin, A.; Chambers, D.; Azevedo, S.; Kalinin, A.; Pevzner, R.; Tokarev, M.; Holsapple, E.; Rama, O.; et al. Development of Ultrasound Tomography for Breast Imaging: Technical Assessment. *Med. Phys.* **2005**, *32*, 1375–1386.
8. Duric, N.; Littrup, P.; Poulo, L.; Babkin, A.; Pevzner, R.; Holsapple, E.; Rama, O.; Glide, C. Detection of Breast Cancer with Ultrasound Tomography: First Results with the Computed Ultrasound Risk Evaluation Prototype. *Med. Phys.* **2007**, *34*, 773–785.
9. Li, C.; Duric, N.; Littrup, P.; Huang, L. In Vivo Breast Sound-Speed Imaging with Ultrasound Tomography. *Ultrasound Med. Biol.* **2009**, *35*, 1615–1628.
10. Sandhu, G.Y.; Li, C.; Roy, O.; Schmidt, S.; Duric, N. Frequency Domain Ultrasound Waveform Tomography: Breast Imaging Using a Ring Transducer. *Phys. Med. Biol.* **2015**, *60*, 5381–5398.
11. Qu, X.; Azuma, T.; Yogi, T.; Azuma, S.; Takeuchi, H.; Tamano, S.; Takagi, S. Synthetic Aperture Ultrasound Imaging with a Ring Transducer Array: Preliminary Ex Vivo Results. *J. Med. Ultrason.* **2016**, *43*, 461–471.
12. Choe, J.W.; Oralkan, O.; Nikoozadeh, A.; Gencel, M.; Stephens, D.N.; O'Donnell, M.; Sahn, D.J.; Khuri-Yakub, B.T. Volumetric Real-Time Imaging Using a CMUT Ring Array. *IEEE Trans. Ultrason. Ferroelectr. Freq. Control.* **2012**, *59*, 1201–1211.
13. Jiang, X.; Xiao, Y.; Wang, Y.; Yu, J.; Zheng, H. Plane Wave Imaging Combined with Eigenspace-Based Minimum Variance Beamforming Using a Ring Array in Ultrasound Computed Tomography. *Biomed. Eng. Online* **2019**, *18*, 7.
14. Wu, Y.; Zhang, W.; Shao, X.; Yang, Y.; Zhang, T.; Lei, M.; Wang, Z.; Gao, B.; Hu, S. Research on the Multi-Element Synthetic Aperture Focusing Technique in Breast Ultrasound Imaging, Based on the Ring Array. *Micromachines* **2022**, *13*, 1753.
15. Ozmen, N.; Dapp, R.; Zapf, M.; Gemmeke, H.; Ruiter, N.V.; van Dongen, K.W.A. Comparing Different Ultrasound Imaging Methods for Breast Cancer Detection. *IEEE Trans. Ultrason. Ferroelectr. Freq. Control.* **2015**, *62*, 637–646.
16. Hasegawa, H.; Nagaoka, R. Initial Phantom Study on Estimation of Speed of Sound in Medium Using Coherence among Received Echo Signals. *J. Med. Ultrason.* **2019**, *46*, 297–307.
17. Nagaoka, R.; Omura, M.; Hasegawa, H. Investigation of a Method to Estimate the Average Speed of Sound Using Phase Variances of Element Signals for Ultrasound Compound Imaging. *J. Med. Ultrason.* **2024**, *51*, 17–28.
18. Rodriguez-Molares, A.; Rindal, O.M.H.; D'HOoge, J.; Masoy, S.-E.; Austeng, A.; Bell, M.A.L.; Torp, H. The Generalized Contrast-to-Noise Ratio: A Formal Definition for Lesion Detectability. *IEEE Trans. Ultrason. Ferroelectr. Freq. Control.* **2020**, *67*, 745–759.
19. Shi, Q.; Li, Y.; Liu, Y.; Gu, M.; Song, X.; Liu, C.; Ta, D.; Wang, W. Index-Rotated Fast Ultrasound Imaging of Cortical Bone Based on Predicted Velocity Model. *IEEE Trans. Ultrason. Ferroelectr. Freq. Control.* **2022**, *69*, 1582–1595.
20. Fincke, J.; Zhang, X.; Shin, B.; Ely, G.; Anthony, B.W. Quantitative Sound Speed Imaging of Cortical Bone and Soft Tissue: Results from Observational Data Sets. *IEEE Trans. Med. Imaging* **2022**, *41*, 502–514.
21. Wiskin, J.; Malik, B.; Klock, J. Low Frequency 3D Transmission Ultrasound Tomography: Technical Details and Clinical Implications. *Z. Med. Phys.* **2023**, *33*, 427–443.
22. Shi, Q.; Zhou, T.; Liu, Y.; He, Y.; Shi, L.; Li, Y.; Ta, D. A 3-D Ultrasound Tomography Method for Bone Morphology Evaluation. *IEEE Trans. Comput. Imaging* **2024**, *10*, 17–27.
23. Li, Z.; Sun, Y.; Li, L.; Yao, Z.; Yin, X.; Yuan, J. Radius-Adjustable Ring Ultrasound Transducer Array for Real-Time 3D Imaging of Large Volume Targets. *Ultrasound Med. Biol.* **2025**, *51*, 2161–2172.
24. Hou, Z.; Wu, F.; Gao, D.; Wang, R.; Zhang, G.; He, C.; Cui, J.; Zhang, W.; Yang, Y.; Jia, L. Development of a 1 × 512 Ring Transducer Array-Based 3D Ultrasound Imaging System for Accurate Breast Lesion Detection: Phantom and Preliminary Clinical Feasibility Study. *Micromachines* **2026**, *17*, 223.
25. Zuo, X.; Wang, H.; Yuan, X.; Gao, D.; He, C.; Wang, Y.; Yang, R.; Ren, R.; Zhang, W. Rapid High-Resolution Breast Imaging with Ring-Array Multi-Subarray Synthetic-Aperture Frequency-Domain Ultrasound Computed Tomography Method. *IEEE Trans. Instrum. Meas.* **2026**, *75*, 4503818.
26. Garrett, D.C.; Xu, J.; Oh, D.; Aborahama, Y.; Ku, G.; Maslov, K.; Tseng, W.W.; Wang, L.V. Whole Cross-Sectional Human Ultrasound Tomography. *Nat. Biomed. Eng.* **2026**. https://doi.org/10.1038/s41551-026-01660-4
27. Zeng, J.; Lou, D.; Zhang, Q.; Zhang, H.; Zhu, H.; Cheng, X.; Wang, T.; Xu, S.; Ling, Y.; Ding, M. Echo Intensity Correction Method for Ultrasound Computed Tomography in Musculoskeletal Imaging. *Bioengineering* **2026**, *13*, 352.
28. Littrup, P.J.; Duric, N.; Sak, M.; Li, C.; Roy, O.; Brem, R.F.; Larsen, L.H.; Yamashita, M. Multicenter Study of Whole Breast Stiffness Imaging by Ultrasound Tomography (SoftVue) for Characterization of Breast Tissues and Masses. *J. Clin. Med.* **2021**, *10*, 5528.
29. Malik, B.; Terry, R.; Wiskin, J.; Lenox, M. Quantitative Transmission Ultrasound Tomography: Imaging and Performance Characteristics. *Med. Phys.* **2018**, *45*, 3063–3075.

30. Zhang, Q.; Guo, X.; Zhang, L.; He, J.; Liu, Q.; Mao, L.; Xu, Y.; Ding, M.; Yuchi, M.; Ma, B. Real-Time Reflection Imaging System for Ultrasound Computed Tomography with a Circular Ring Array. *IEEE Sens. J.* **2025**, *25*, 29830–29840.
31. Duric, N.; Littrup, P.; Schmidt, S.; Li, C.; Roy, O.; Bey-Knight, L.; Janer, R.; Kunz, D.; Chen, X.; Goll, J.; et al. Breast Imaging with the SoftVue Imaging System: First Results. *Proc. SPIE Int. Soc. Opt. Eng.* **2013**, *8675*, 86750K.
32. Cianca, J.; Patel, S.I. *Musculoskeletal Ultrasound Cross-Sectional Anatomy*; Springer Publishing Company: New York, NY, USA, 2017.

Disclaimer/Publisher's Note: The statements, opinions and data contained in all publications are solely those of the individual author(s) and contributor(s) and not of MDPI and/or the editor(s). MDPI and/or the editor(s) disclaim responsibility for any injury to people or property resulting from any ideas, methods, instructions or products referred to in the content.